

Characterization of Manganese Acetate Hydrate Solutions and Their Potential Use for Energy Storage Applications

Chalal Tachouaft,^[a] Hamza Kahri,^[a] Liwen Wang,^[b] Georgios Nikiforidis,^[b] and Mériem Anouti^{*[a]}

While there have been numerous studies on the use of manganese acetate for electrode manufacture, scarce reports exist on the utility of manganese acetate electrolytes for energy storage applications. This study provides a comprehensive understanding of the thermal, volumetric, and transport properties of manganese acetate hydrate solutions and highlights their potential for use in energy storage applications. Noteworthy thermal behaviours, phase transitions, and strong interactions between manganese cations, acetate anions, and water molecules are observed. Transport properties reveal salt concentration's impact ($0.4\text{--}3.9\text{ mol L}^{-1}$) on viscosity and conductivity, with higher concentrations ($>2.5\text{ mol L}^{-1}$) indicating increased interaction. The non-Arrhenius behaviour in conductivity is elucidated using the Vogel-Fulcher-Tamman model, accentuating the unique properties of these solutions com-

pared to other aqueous electrolytes due to the role of acetate ligands. The formulated two-electrode symmetric supercapacitors exhibit pseudocapacitive behaviour, reversible redox reactions ($\text{Mn}^{2+}/\text{Mn}^{3+}$), and salt concentration-dependent specific capacitance. Manganese acetate as an electrolyte leads to reversible manganese dioxide deposition, with its concentration affecting redox reactions and capacitance. Molecular simulations support the observed electrochemical performance, emphasizing the Mn^{2+} -acetate complexation. Long-term cycling experiments demonstrate stability over 2000 cycles, with a stable specific capacitance of 130 F g^{-1} and a gradual coulombic efficiency decrease (~97%). The results of this work underscore the potential of manganese acetate hydrate solutions as a stable, effective and green electrolyte for energy storage applications.

1. Introduction

The intermittent nature of renewables, such as solar and wind, poses challenges to maintaining a stable and consistent power supply. Energy storage technologies act as a vital buffer, storing excess energy during peak generation periods and releasing it when demand is high or renewable sources are unavailable.^[1] Supercapacitors represent one of the most reliable and cost-effective solutions.^[2] To enable their large-scale deployment, it is imperative to employ cost-effective, durable safe materials and electrolytes,^[3] especially aqueous ones (for the latter) since they are intrinsically safe and compatible. With regards to stable materials in neutral aqueous electrolytes, activated carbon (AC) and manganese dioxide (MnO_2) in symmetrical,^[4] asymmetrical,^[5] or hybrid^[6] systems have been successfully implemented.

Activated carbon (AC) is a widely used material for supercapacitor applications due to its low manufacturing cost and high surface area.^[7] In this material, the energy storage is capacitive and involves the formation of a double layer.^[8] In the case of manganese oxide, MnO_2 , energy storage can exhibit a pseudo-capacitive behaviour by cation intercalation (H^+ , Na^+ , Li^+) from the electrolyte,^[9,10] while it can undergo conversion electrochemical reactions via the redox $\text{Mn}^{3+}/\text{Mn}^{2+}$ couple.^[11] In contrast to intercalation-type reactions, conversion ones offer high operating voltage, specific capacitance, and fast kinetics, mitigating the limitations of insertion materials on such energy storage devices.

The deposition/dissolution reaction of MnO_2 is a solid-liquid phase conversion reaction with its potential dependent on protons.^[12] Due to its high redox potential (1.23 V vs. SHE) and theoretical capacity (616 mAh g⁻¹ for a 2e⁻ reaction), this material has garnered significant attention in recent years, particularly in battery applications such as zinc/manganese dioxide (Zn/MnO_2) batteries.^[13] The conversion process involves the generation of protons during the deposition of MnO_2 and necessitates a constant proton concentration for the reverse dissolution reaction.^[11,13] Solid MnO_2 deposits onto the carbon felt or graphite fibre electrode from Mn^{2+} ions during constant voltage charging, dissolve reversibly into Mn^{2+} ions in the electrolyte, yielding great stability.^[14]

Supercapacitors based on activated carbon are easy to manufacture and cost-effective.^[15] When associated with MnO_2 and neutral aqueous electrolytes, they are attractive due to their robust performance and minimal environmental impact. Indeed, in terms of environmental and cost considerations,

[a] C. Tachouaft, H. Kahri, M. Anouti

Laboratoire PCM2E, Université de Tours, Parc de Grandmont, 37200 Tours, France

E-mail: meriem.anouti@univ-tours.fr

[b] L. Wang, G. Nikiforidis

Advanced Sustainable Materials Laboratory, Institute for Materials Discovery East, University College London East, Marshgate, 7 Sidings Street, Stratford, London, E20 2AE

Supporting information for this article is available on the WWW under <https://doi.org/10.1002/batt.202300560>

© 2024 The Authors. Batteries & Supercaps published by Wiley-VCH GmbH. This is an open access article under the terms of the Creative Commons Attribution License, which permits use, distribution and reproduction in any medium, provided the original work is properly cited.

electrochemical manganese dioxide (EMD) is likely to remain the preferred energy material^[16] for alkaline and lithium batteries. Still, the recycling of their components can be challenging, especially lithium, potassium, sulfur and nitro-compounds (that stem from material and electrolytes such as Na_2SO_4 , LiNO_3 and KCl).^[17] Hence, it is highly desirable to explore electrolyte compositions that limit the recovery of the metals.^[18]

Previous studies have demonstrated the use of manganese acetate ($\text{Mn}(\text{Ac})_2$) as a precursor to deposit manganese oxides for energy storage devices, for example, an induced deposition method to prepare multi-walled $\gamma\text{-MnO}_2$ /carbon nanotube composites^[19] and the effects of manganese acetate on the anodic performance of carbon nanotubes for rechargeable Li-ion batteries.^[20] More recently, acetate salts, i.e., $\text{Zn}(\text{CH}_3\text{COO})_2$ with $\text{Mn}(\text{CH}_3\text{COO})_2$, were selected as electrolytic salts to unlock the $\text{Mn}^{4+}/\text{Mn}^{2+}$ two-electron redox reaction, considering the adsorption effect of acetate (CH_3COO^-) ions as a solution for the formation of Zn dendrites and the poor thermodynamic and electrochemical stability of the Zn anode in aqueous electrolytes.^[21] Although several works highlight the advantages of using $\text{Mn}(\text{Ac})_2$ as an additive or precursor, no work describes to our knowledge, its use as an electrolyte for energy storage.

To this end, building on the recent breakthrough, where, for the first time, another manganese-based salt ($\text{Mn}(\text{NO}_3)_2$, manganese nitrate) was presented as an electrolyte in AC/ $\text{Mn}(\text{NO}_3)_2$ /AC supercapacitors,^[22] we present the utilization of $\text{Mn}(\text{CH}_3\text{COO})_2$ salt for a similar supercapacitor type. This salt serves a dual purpose by facilitating in-situ MnO_2 deposition on the cathode and acting as an electrolyte for a similar-type AC// MnO_2 supercapacitor. The outcomes showcase commendable specific capacitance (130 Fg^{-1} for a cell voltage of 1.0 V) and cycleability (2000 cycles). Notably, considering the environmentally friendly nature of the electrolytes explored in this investigation, the significance of green energy storage devices is underscored in this study.

Experimental

Solvent, salt and electrolyte preparation

Table 1 outlines the compositions of the different devised electrolytes. The manganese (II) acetate tetrahydrate (Sigma Aldrich, >99%, $T_m=80^\circ\text{C}$, pH = 7) was used as received.

Electrolyte Characterization

The ionic conductivities were performed in single sealed cells using a BioLogic[®] multichannel conductometer based on a frequency

response analyzer (MCM 10) connected to a Peltier-based temperature control unit (-10 to 80°C). The conductometer was calibrated before any measurement using a standard potassium chloride (KCl) solution. Dynamic viscosity and density of the samples were measured using an Anton Parr densitometer comprising a digital vibrating tube densitometer (model 60/602, Anton Parr, France) coupled with an Anton Parr rolling-ball viscometer (Lovis 2000 M/ME, Anton Parr, France). The densitometer/viscometer was calibrated before measurements with ultra-pure water over a temperature range from 10 to 60°C . Differential scanning calorimetry (DSC) was performed with a PerkinElmer DSC 4000 for all the samples. Samples, initially at 25°C , were cooled to -60°C followed by a five-minute isothermal plateau at this temperature and then heated up to 250°C . Each scan was performed at 5°C min^{-1} .

Supercapacitor assembly

Activated carbon (AC) coated on aluminium was provided from Blue Solution[®], France and used as positive and negative electrodes of the supercapacitor (SC). The physical and textural parameters of the AC have been described previously.^[23] The AC electrodes had a diameter of 1 cm (geometric surface area of 0.785 cm^2). The separator (Whatman filter paper, GF/C, $\phi=12 \text{ mm}$) and electrodes were dried in a Buchi oven at 80°C for 12 h to remove residual water.

An electrolyte of $200 \mu\text{L}$ was added dropwise from a micropipette (Mettler-Toledo) in between each layer ($50 \mu\text{L}$ on each electrode and $100 \mu\text{L}$ on the separator) for the SC. The reference electrode used for three-electrode cyclic voltammograms was an Ag/Ag⁺ wire (Ossila).

Electrochemical investigation

Galvanostatic charge-discharge (GCD) and cyclic voltammetry (CV) were performed by a Biologic potentiostat using a three-electrode Swagelok[®] cell. CV plots were performed relative to the set electrochemical window at designated scan rates and normalized with respect to the active mass of the activated carbon (i.e., $\sim 4.6 \text{ mg}$). The specific capacitance (Fg^{-1}) of the two-electrode symmetric supercapacitor was determined according to equations reported in previous studies.^[24]

Materials Characterization

Ex-situ characterization of the cathode, anode and separator of the devised supercapacitors was carried out. The Raman spectra of the activated carbon electrodes were obtained inVia[™] confocal Raman microscope (Renishaw) under a 532 nm laser excitation and a $10\times$ magnification lens. The deconvolution of the D and G bands was done by Lorentzian fitting. The XRD spectra of the carbon electrodes were collected from a D8 Advance (Bruker) using Ni-filtered Cu K α (1.54 \AA , generator: 40 kV , 40 mA) radiation, equipped with a Lynx-eye detector (2θ range from 10 to 90° in continuous mode

Table 1. Composition of the $\text{Mn}(\text{Ac})_2\text{-H}_2\text{O}$ aqueous solutions in mass ratio, w ; molal concentration in salt, \mathcal{M} and Mn^{2+} molar concentration C .

Solution	S1	S2	S3	S4	S5	S6
w (%) in mass	0.1	0.2	0.3	0.4	0.5	0.8
\mathcal{M} (mol kg^{-1})	0.64	1.45	2.48	3.85	5.78	*
$C_{(\text{Mn}^{2+})}$ (mol L^{-1})	0.37	0.87	1.57	2.55	3.86	*

* S6 is a supersaturated solution used solely for differential scanning calorimetry measurements.

and step size of 0.02). Top-view electron microscopy pictures of the electrodes were acquired by a focused ion beam (FIB) SEM (FEI Helios NanoLab 400S) using a gallium ion source. XRD (X-ray Diffraction) analysis of the activated carbon electrodes was carried out with an X-ray diffractometer (D8 Advance, Bruker). The wavelength of the Cu K α radiation, λ , was 1.54 nm. The cycled GF-C (Whatman) separators were characterized using Fourier Transform Infrared Spectroscopy (FT-IR, Shimadzu IRAffinity-1S) in air. The quantum chemical calculations were carried out by the semi-empirical MOPAC method with the PM6 theory. The molecular orbital energies were calculated with a larger basis Geometry optimization was performed with B3LYP/6-31G under Gaussian software.

2. Results and discussion

2.1. Physical properties

2.1.1. Thermal properties of mixtures

The DSC measurements were carried out between -120 and 80 °C for the six investigated solutions (S1 to S6) and are shown in Figure 1a. The protocol involves an initial cooling from 25 to -120 °C followed by heating from -120 to 80 °C, at a rate of 5 °C min $^{-1}$. The thermograms indicate that four electrolytes (S1-S4) have similar phase transitions. During the cooling phase, we observe a crystallization temperature (T_c) between -20 and -40 °C. This transition is a metastable phenomenon, and it occurs after a supercooled state. Upon heating, the same solutions reveal cold crystallization (T_{cc}), followed by the starting of the melting of the mixture corresponding to the temperature of the eutectic mixture (T_e). Two consecutive peaks can be observed, each corresponding to the dehydration and the unique melting of the hydrated salts.^[25] The mixture finishes its melting at T_m , which drops from -1 to -6 °C for S1 to S4,

respectively. The S5 and S6 electrolytes do not feature any transition phases (i.e., T_{cc} , T_m , T_e) as they approximate the composition of tetrahydrate, dehydrate, and display melting behaviour outside the investigated temperature range (i.e., -60 to 10 °C). In the case of the anhydrous salt, the T_m extends to 102 – 103 °C,^[26] whereas the tetrahydrate salt displays two distinct peaks indicating dehydration at 70 °C and melting at 120 °C.^[25]

The water-ice mixtures with Mn(Ac) $_2$ exhibit a eutectic-like behaviour, consistent with observations in other hydrates.^[27] Combining the T_m and T_e values from Figure 1 and the melting temperatures of water (0 °C) and tetrahydrate manganese acetate salt (Mn(Ac) $_2$ ·4H $_2$ O with T_m ~80 °C),^[25] an isobaric eutectic diagram of the Mn(Ac) $_2$ -ice system is realized (red curve of Figure 1b). As a comparison, the diagram of the Mn(NO $_3$) $_2$ -ice mixture (black curve in Figure 1b) is also included. The eutectic depth (ΔT , the ideality line connecting the melting temperatures of water and the tetrahydrate salt and the eutectic temperature) reaches 93 °C, and is greater than its counterpart Mn(NO $_3$) $_2$ -H $_2$ O (ΔT =65 °C),^[22] suggesting a stronger amplitude of interactions between species (anion-H $_2$ O) in the eutectic mixture.^[28]

All electrolytes reveal cold crystallization temperatures (T_{cc}) suggesting that the molecules contain a rigid core and flexible fragments (i.e., acetate anions)^{[29], [30]} which in turn, increase the degree of freedom. The molten state consists of several isomers that can undergo structural changes, disrupt the uniformity of the system and prevent its crystallization.^[31] The Mn(Ac) $_2$ -(H $_2$ O) system (S1-S4) presents ionic liquid crystal characteristics, where the charged ions exhibit high degrees of translational and rotational ionic mobilities appropriate for cold crystallization.^[32] Acetates serve as flexible ligands, whereas water molecules function as rigid ligands. This distinction can be attributed to the charge delocalization on the carboxyl (COO $^-$) group, explaining the combination of a rigid nucleus Mn(H $_2$ O) $_4$ and

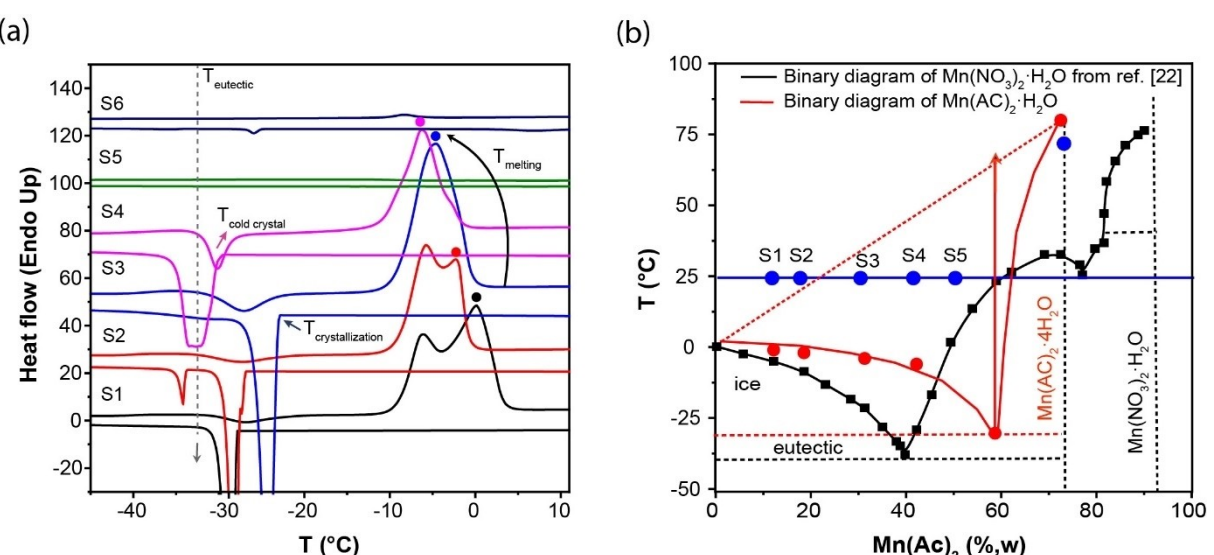


Figure 1. (a) Thermograms of the solutions of Table 1 (S1–S6). (b) Eutectic diagram of the aqueous acetate solution constructed with the aid of Ref.^[22] incorporating the position of the six electrolytes used in this study (S1–S6).

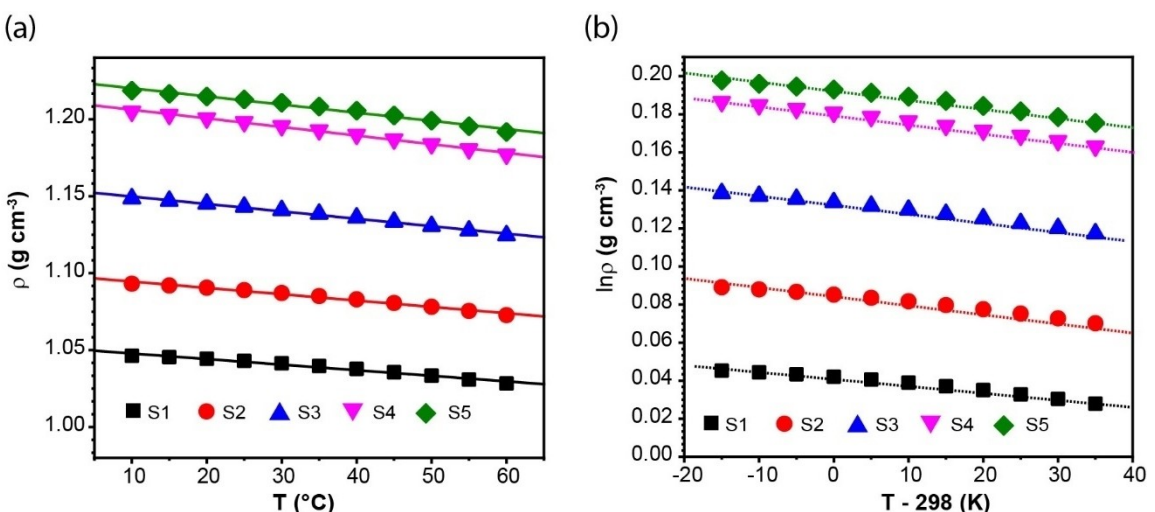


Figure 2. (a) Evolution of density as a function of temperature for the $\text{Mn}(\text{AC})_2\text{-H}_2\text{O}$ system, i.e., S1–S5 solutions. (b) Modelling of density versus temperature for the same solutions.

two flexible acetates.^[33] Therefore, compounds of this type have long phases of partial order disrupted by molecular movement^[33] which prevents any phase transition from being seen, as evidenced in the S5 and S6 solutions (Figure 1a).

2.1.2. Volumetric and transport properties of the eutectic mixture

2.1.2.1. Volumetric properties

The densities of the solutions (S1 to S5) were measured at atmospheric pressure between 10 and 55 °C and are presented in Figure 2a. The molecular volume (V_m) determined at 25 °C according to Equation 1^[34] is given in Table 2.

$$V_m = \frac{M}{\rho \times N_A} \quad (1)$$

where M denotes the molar mass of the solution, ρ is the density and N_A is the Avogadro constant. The V_m values lie between 19 and 32 cm 3 mol $^{-1}$ and increase with higher salt concentration. The variation in density with temperature is modelled by Equation 2^[34] below:

$$\alpha = - \left(\frac{\partial \ln(\rho)}{\partial T} \right)_p \quad (2)$$

where α is the coefficient of thermal expansion that reflects the restructuring ability of the solution under thermal agitation.

The α values (-3.63 to -5.31×10^{-4} K $^{-1}$, Table 2) are typical of systems containing self-associated molecules such as ionic liquids^[35] and are higher than the one of liquid water viz. -2.0×10^{-4} K $^{-1}$.^[36] The intermolecular interactions between the manganese cation, water and acetate anions promote stacking efficiency and a self-association domain in the liquid. This observation suggests that there are stronger such interactions in the formulated eutectic mixture than in standard electrolytes.

What's more, applying Glasser's theory,^[37] Equations 3 and 4 were employed to ascertain the standard molar entropy (S°) and internal energy (U_{pot}) of the investigated electrolytes. The coefficients X1, X2, Y1 and Y2 are evaluated for a series of mono or divalent salts according to the stoichiometry of the salt.^[38] The standard values of S° and U_{pot} for each solution at 25 °C are listed in Table 2.

$$S^\circ = X1 (V_m/nm^3) + Y1 ; X1 = 1597; Y1 = 46 \quad (3)$$

$$U_{pot} = X2 \left(\frac{\rho}{M} \right)^{1/3} + Y2 ; X2 = 6765; Y2 = 365 \quad (4)$$

S° and U_{pot} are related to the self-organization capacity of the solution according to the stoichiometry of the salt (i.e., AB, AB₂ or A₂B) for unknown or hypothetical anhydrous materials whose solvates are known.^[39] The decrease of the S° values from S1 to S5 reflects the ability of the solution(s) to reorganize in the presence of high quantities of salt under temperature variation. Compared to liquid water ($S^\circ = 69.9$ K J K $^{-1}$ mol $^{-1}$) and ice ($S^\circ = 44.7$ K J K $^{-1}$ mol $^{-1}$),^[40] they are less organized pointing out that the pattern of molecular interactions between the formulated eutectic solutions (S1–S5) and the standard aqueous

Table 2. Volumetric and thermodynamic properties of the $\text{Mn}(\text{AC})_2\text{-H}_2\text{O}$ solution at 25 °C, following the pseudo-crystal lattice model (Equations 1–4).

Properties	S1	S2	S3	S4	S5
$10^{-4} \times \alpha$ (K $^{-1}$)	-3.63	-4.11	-4.82	-5.60	-5.30
V_m (cm 3) at 25 °C	17.28	16.57	15.81	15.11	14.98
S° (J mol $^{-1}$ K $^{-1}$) ± 1	92	90	88	87	86
U_{pot} (kJ mol $^{-1}$) ± 30	1597	1614	1635	1655	1660

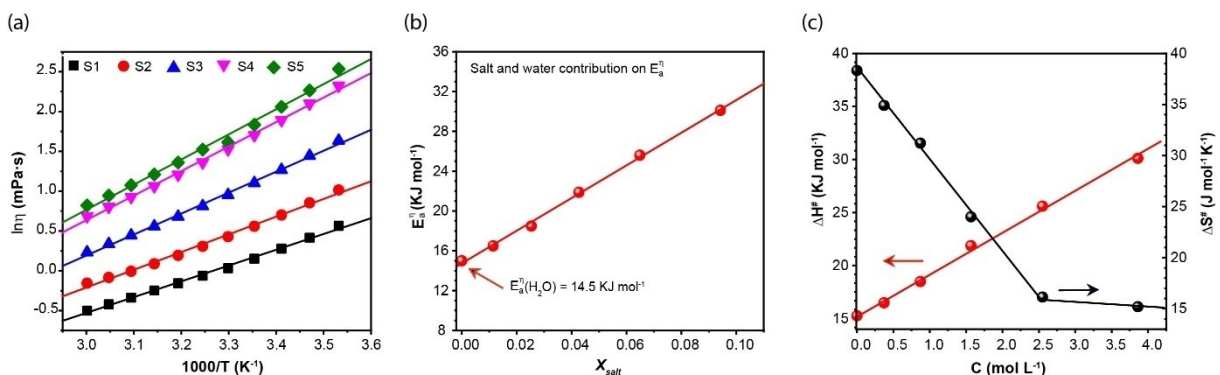


Figure 3. (a) Evolution of viscosity with temperature for different $\text{Mn}(\text{AC})_2\text{-H}_2\text{O}$ solutions (S1–S5 solutions). (b) Arrhenius equation modelling of the dynamic viscosity. (c) Enthalpy and entropy of activated state for the $\text{Mn}(\text{AC})_2\text{-H}_2\text{O}$ system (S1–S5).

electrolytes is not the same. On the other hand, the lattice energies (U_{pot}) unveil meagre variation from S1 to S5 and are comparable to those reported for hydrate salts of the same nature with bivalent cations, such as calcium chloride tetrahydrate, $\text{Ca}(\text{Cl})_2\cdot 4\text{H}_2\text{O}$ ($U_{pot} \sim 2200 \text{ kJ mol}^{-1}$) and calcium iodide, $\text{Ca}(\text{I})_2$ ($U_{pot} \sim 1800 \text{ kJ mol}^{-1}$).^[38]

2.1.2.2. Transport properties

The decreasing variation of the dynamic viscosity of the solutions with elevated temperature (10–60 °C) is highlighted in Figure 3a. Figure 3b presents the viscosity as a function of temperature following the Arrhenius law^[41] (Equation 5). From the linear fitting, the activation energy (E_a^η) of the viscous flow is extracted. The latter varies linearly with the mole fraction of salt, x_{salt} (Equation 6, Figure 3b), enabling the distinguishing of the salt contribution (E_{salt}^η) from the solvent one (E_0^η).^[42]

$$\eta = \eta_0 \exp\left[-\frac{E_a^\eta}{RT}\right] \quad (5)$$

$$E_a^\eta = E_0^\eta + x_{salt} E_{salt}^\eta \quad (6)$$

The E_0^η values obtained at infinite dilution closely align with those reported for water, $\sim 16 \text{ kJ mol}^{-1}$.^[43] This corresponds to the energy needed to break two hydrogen bonds (i.e., 8.4 kJ mol^{-1} for H-bond) and the tetrahedral pentamer of water.^[44] With the addition of salt, this value increases, implying that the interactions are stronger in the water/salt mixture. In the most concentrated solution (S5), the energy is double that of pure water signifying twice as many interactions.

Furthermore, according to Eyring's theory,^[45] the liquid structure can be considered a quasi-crystal network where the molecules move in the liquid state in parallel layers by sliding planes. Each species first acquires enough energy to overcome the activation energy barrier and jump into a new "hole". The energy barrier is the activated state in which an available vacant site (hole) depends on the organization of the solution and the interaction forces in the sense of the solution. This is assimilated to the variation of Gibbs energy and can be expressed into

enthalpy (interactions) and entropy (disorder) of the transient state (Equation 7).^[45] The values obtained for the S1–S5 solutions are given in Figure 3c and detailed in Table 3, thereby providing experimental insights into the theoretical framework proposed by Eyring.

$$\eta = \frac{hN_A}{V_m} \exp\left(\frac{\Delta S^\ddagger}{R}\right) + \exp\left(\frac{\Delta H^\ddagger}{RT}\right) \quad (7)$$

From Figure 3c, the activation entropy (ΔS^\ddagger) decreases as the amount of salt increases. The formation of holes is easier and up to a certain salt concentration (3.85 mol L^{-1}) has a marked structuring effect. Beyond solution S4, the entropy no longer varies. The ΔS^\ddagger values are in accordance with those of reported aqueous electrolytes containing magnesium sulfate, sodium carbonate and copper nitrate ($16\text{--}32 \text{ J mol}^{-1} \text{ K}^{-1}$)^[46] and lower by a factor of two to those of organic solvents (ethylene and propylene carbonate).^[42] As expected, the low-concentrated solution (S1) has a similar value to the one of water, i.e., $38 \text{ J mol}^{-1} \text{ K}^{-1}$.

Additionally, the variation in viscosity with concentration modelled by the Jones-Dole-Kaminsky equation (JDK, Equation 8)^[47] is illustrated in Figure 4a. The polynomial adjustment parameters A , B and D stem from the ratio

$\eta_r = \left(\frac{\eta}{\eta_0}\right) = f(C)$, where η and η_0 are the viscosities of the solutions investigated and of pure water, respectively.^[48,49] The solute-solvent short-distance interactions parameter (B) is derived from Equation 9,^[47,50] which in turn leads to the effective hydrodynamic radius r_H (Equation 10, Figure 4b).^[47] The latter comes from Einstein's theory on the model of solid spheres in solution and the solvent crown around solvated ions.^[51]

Table 3. Activation enthalpy ΔH^\ddagger and entropy ΔS^\ddagger for viscous flow of the $\text{Mn}(\text{AC})_2\text{-H}_2\text{O}$ system.

Solution	S1	S2	S3	S4	S5
$\Delta H^\ddagger (\text{kJ mol}^{-1}) \pm 0.05$	16.4	18.4	21.8	25.6	30.1
$\Delta S^\ddagger (\text{J mol}^{-1} \text{ K}^{-1}) \pm 0.05$	38.3	34.9	31.2	16.1	15.2

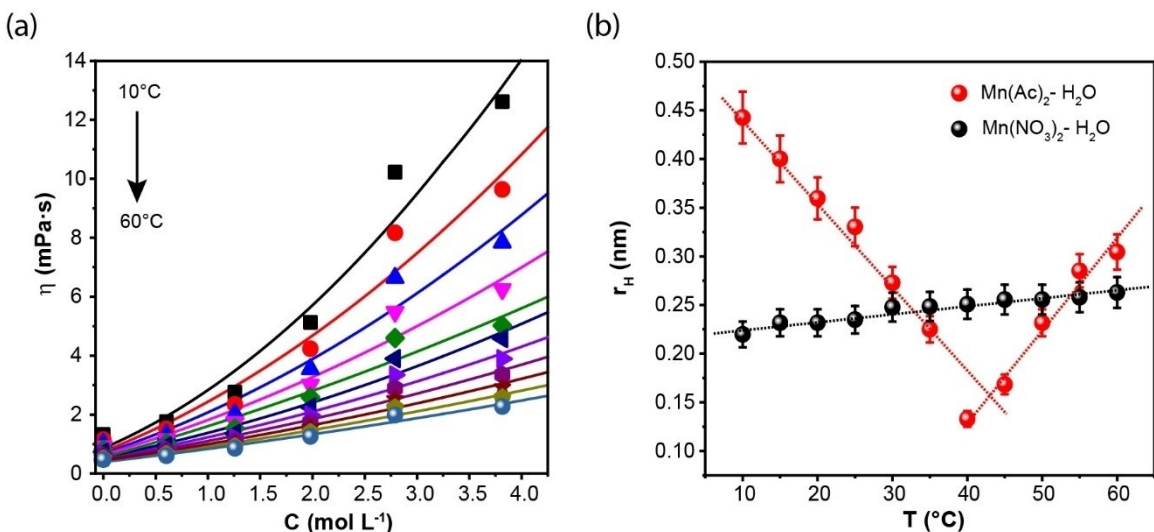


Figure 4. (a) Dynamic viscosity at different concentrations and (b) Effective hydrodynamic radius of the $\text{Mn}(\text{AC})_2 \cdot \text{H}_2\text{O}$ system. The $\text{Mn}(\text{NO}_3)_2 \cdot \text{H}_2\text{O}$ system from ref.^[22] is displayed here for comparison purposes.

$$\eta_r = 1 + A\sqrt{C} + BC + DC^2 \quad (8)$$

$$B = 2.5 \left(\frac{4}{3} \pi r_H^3 N_A \right) \quad (9)$$

$$r_H = \sqrt[3]{\frac{3}{10 \times \pi \times N_A}} \quad (10)$$

Between 10 and 60°C, the positive B -coefficient values (Figure 4a) signify that the salt has a structuring effect on the solvent, thereby augmenting the organization of the solution. The radius r_H for the $\text{Mn}(\text{Ac})_2 \cdot \text{H}_2\text{O}$ complex derived from Equation 10 lies between 150 and 450 pm (Figure 4b), and was found to be highly dependent on temperature. More specifically, r_H decreases up to 40°C (150 nm) followed by a subsequent increase. The hydration radius (conformed to a single crown of water) is the result of the cross interactions between the water and the manganese cation, and it involves the acetate anion bound by hydrogen bonding to water molecules and by electrostatic interactions with the cation. The competition between such interactions leads to an inflection point at ~40°C. The r_H values in the temperature range of 30 to 50°C are similar to the ones reported for the manganese nitrate salt^[22] and at lower temperatures (10–25°C) twice as large. In water and at 25°C, the r_H for $\text{Mn}^{2+} \cdot \text{H}_2\text{O}$ values are of the same order of magnitude as the ones reported in aqueous solution for alkali cations, such as lithium, sodium and potassium.^[52]

What's more, the ionic conductivities of these aqueous systems were investigated between -10 and 80°C in three cycles. Starting at room temperature, the process involves cooling down to -10°C, then raising the temperature to 80°C, and finally returning to a state of thermodynamic equilibrium at 25°C. Solutions S1 and S5 (Figures 5a and 5b) subjected to the same cycling protocol reveal different appearances. For S5 (the more concentrated solution), a monotonic increase in conductivity from -20 to 80°C is evident, while for S1 a break in

the variation of conductivity became apparent at 3°C (Figure 5a). This finding is consistent with the thermograms of Figure 1 where the most concentrated solution (S5, 3.86 mol L⁻¹) did not display the characteristic of cold crystallization, unlike the rest (S1–S4).

From Figure 5c, the electrolytes demonstrate a non-Arrhenius behaviour, i.e., the relationship is non-linear over the studied temperature range.^[53] Thus, the Vogel-Fulcher-Tamman (VFT) model is applied (Equation 11)^[54] adjusting temperature variations through the use of a corrective term T_0 , the ideal glass temperature.^[55] The pseudo-activation energies B_σ^σ for ionic mobility extracted from the VFT model fitting, increase with higher salt concentration, yet are 15 times lower than the values obtained from alkaline salts in water (i.e., 10–15 kJ mol⁻¹).^[52] This difference derives from the effect of the acetate ligand that alters the van der Waals interactions and the hydrogen bonding in water.^[56] The T_0 values (~203 K) from the VFT model are similar for the S1–S5 solutions (Table 4), and close to the experimental values of glass transition of water ice.^[57,58] The S5 solution (highly concentrated medium) has a lower glass transition and a bigger B value, leading to a greater activation energy in the VFT model.

$$\sigma = \sigma_0 \exp \left[\frac{B_\sigma}{T - T_0} \right] \quad (11)$$

The conductivity is a balance between the mobility of the charge carriers (in this case, Mn^{2+} and CH_3COO^-) and the viscosity of the solution. At low concentrations, the ion mobility increases in proportion to salt concentration and reaches a maximum when the viscosity induced by ion-solvent interactions becomes too high, hindering their diffusion. This inflection point (C_{max} σ_{max}) varies depending on the salt and solvent. For instance, for monovalent cation salts in water such as lithium acetate, the C_{max} lies between 3 and 5 mol L⁻¹ and the σ_{max} arrives at 37 mS cm⁻¹ at a concentration of 3.5 mol L⁻¹.^[59] In the

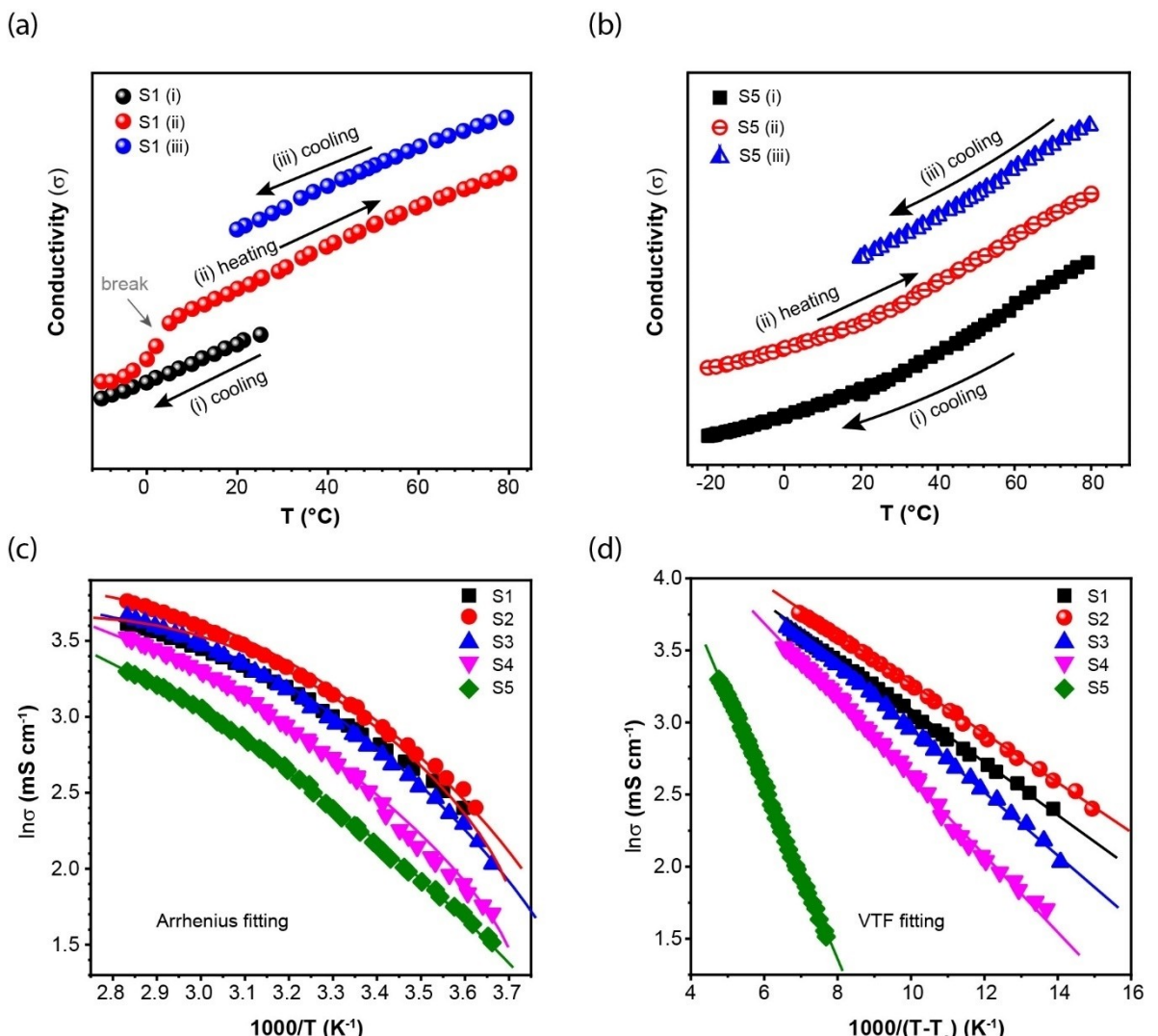


Figure 5. Ionic conductivity variation with temperature for the (a) S1 and (b) S5 solutions. (c) Modelling of ionic conductivity by the Arrhenius equation. (d) Modeling of the Vogel-Fulcher-Tamman (VFT) correlation.

Table 4. Arrhenius parameters for viscosity, VTF fitting parameters for the conductivity and ionicity from Walden's rule.

Solution	Viscosity	Conductivity	Walden rule and ionicity	Dissociation coefficient (α)	
	E_a^η (kJ mol $^{-1}$) ± 0.02	T_0 (K)	B_a^η (kJ mol $^{-1}$) ± 0.05	$W = \sigma \times \eta$ at 25 $^{\circ}\text{C}$ (mS cm^{-1} mPa s)	
S1	16.49	206	-0.17	22	0.85
S2	18.49	209	-0.17	38	0.85
S3	21.87	202	-0.21	52	0.73
S4	25.60	200	-0.26	61	0.77
S5	30.11	143	-0.63	75	0.73

case of Mn(Ac) $_2$, σ_{max} attains 35 mS cm^{-1} at a much lower salt concentration, i.e., 0.8 mol L $^{-1}$ (Figure 6a).

The inherent connection between conductivity and viscosity, which varies in response to changes in temperature is given by the "Walden product" $^{[42,60,61]}$ (Figures 6a and 6b, Table 4). At a given temperature, the Walden product (W) increases going

from S1 to S4 and then decreases for S5. For the latter, the higher viscosity impedes ion mobility and does not compensate for the increase in charge carriers. W drops with elevated temperatures for all solutions (e.g., from 80 mS cm^{-1} mPa s $^{-1}$ at 10 $^{\circ}\text{C}$ \rightarrow 55 mS cm^{-1} mPa s $^{-1}$ at 60 $^{\circ}\text{C}$ for S4, Figure 6b) due to enhanced ion mobility. This implies that the charge carriers

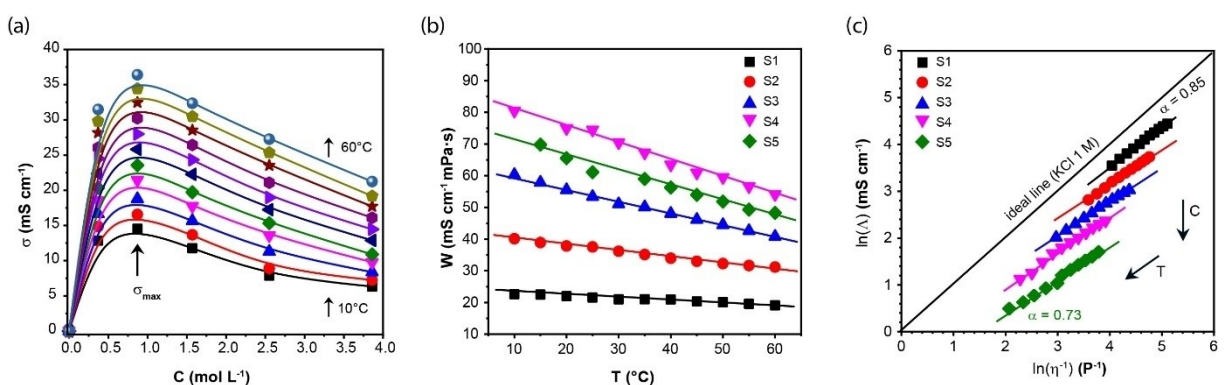


Figure 6. (a) Ionic conductivity variation with concentration from 10 to 60 °C of the $\text{Mn}(\text{Ac})_2\text{-H}_2\text{O}$ complex. (b) Walden product and (c) Ionicity according to the Walden-Angell plot for the $\text{Mn}(\text{Ac})_2\text{-H}_2\text{O}$ system.

stemming from the dissociation of the salt are highly coordinated by the aqueous solvent. This ionic dissociation and ionic mobility can be evaluated by the "Walden-Angell plot",^[62] based on the normalization of molar conductivity as a function of viscosity (Figure 6c). This approach provides a quantitative descriptor, namely "ionicity" and enables us to assess the extent to which the electrolyte diverges from its theoretically predicted ideal ionic state as per the Nernst-Einstein equation. The ideal case is represented by an aqueous potassium chloride solution (KCl, at 0.01 mol L⁻¹) since it exerts a total dissociation.^[62] Deviation from the ideal line signifies a gradual reduction in the ionic nature of the solution.

Angell extended the Walden relationship by introducing the "fractional Walden rule" $((\sigma \times \eta)^\alpha)$ ^[63] where α is a constant that expresses the dissociation rate of the salt ($0 < \alpha < 1$). From Table 4 and Figure 6c, α varies between 0.73 (S5) and 0.83 (S1), so a major part of the salt is dissociated. Considering the primary criteria outlined for low-temperature aqueous electrolytes,^[52] which include a low activation energy, a small hydration radius, substantial supercooling capacity, and effective mediator redox ability, the intermediate manganese hydrate solution S3 appears to meet all these specifications. Yet, it is equally important to look into the weakly (S1, S2) and highly concentrated (S5) domains and highlight any differences that arise due to manganese salt concentration. This scrutiny will be conducted through electrochemical characterization on the following stages of this work.

Overall, the results obtained here shed light on the ionicity of the solutions but do not allow us to visualize and define the type of complexes formed in the solution. Former X-ray scattering and ¹³C NMR spectroscopy^[64] studies in concentrated $\text{Mn}(\text{Ac})_2$ aqueous solutions have validated the formation of complexes between Mn^{2+} cations, and the complexing organic ligand acetate. To be more precise, the analysis of experimental data employed two distinct models one positing the binding of acetate ions to Mn^{2+} cations (Model I) and the other suggesting their lack of binding to Mn^{2+} cations (Model II). Model (II) (Figure S1) agreed with experimental data in concentrated solutions showing the formation of cation hydrate-acetate complexes as well as anion-solvent interactions while Model (I) predominates in dilute solutions. This hypothesis is consistent

with the results of the Walden plot (Figure 6) in terms of ionic association.

2.2. Application of the $\text{Mn}(\text{Ac})_2$ aqueous solution to a supercapacitor

2.2.1. Three-electrode cyclic voltammetry on activated carbon (AC) electrodes

In a symmetric AC|AC electrochemical double-layer supercapacitor, the two electrodes adsorb the same ions (cations for the negatively polarized electrode and anions for the oppositely polarized electrode) at each charge. It is therefore practical before testing the operation and performance (e.g., electrochemical window and specific capacitance) of the supercapacitor, to monitor the potential of each of the two electrodes in a three-electrode system, implementing a silver wire that serves as a pseudo-reference electrode. Figure 7a shows two voltammograms of the S5 solution. The progressive polarization of the negative electrode reveals a classical almost rectangular appearance of the cyclic voltammetry (CV) curve with a stability close to -1.0 V versus Ag/Ag^+ . The positive electrode displays a reversible peak (in the first three CV cycles), indicative of a pseudocapacitive mechanism^[65,66] (i.e., redox reactions at the electrode-electrolyte interface) that however fade in a short time span (<3 minutes), giving rise to a capacitive-like behaviour.

Figure 7b explores the electrochemical window (denoted as E_{cell}) gradually increased from 0.5 to 1.5 V for supercapacitors comprising S2 and S5 solutions, respectively. The effect of concentration is evident here, as the less salt-dense electrolyte (S2) does not reveal an oxidative current, just the common capacitive plot of an electrochemical double-layer capacitor (fill factor > 84%).^[67] On the other hand, the concentrated S5 electrolyte unveils an oxidative current (i.e., oxidation of Mn^{2+} described in Reactions 1 and 2 below) followed by a reduction peak, at an E_{cell} greater than 1.05 V vs Ag/Ag^+ , especially in the initial parts of the cycling process. The oxidative current in Figure 7c originates from a redox reaction that involves the deposition of manganese oxide from the oxidation of Mn^{2+}

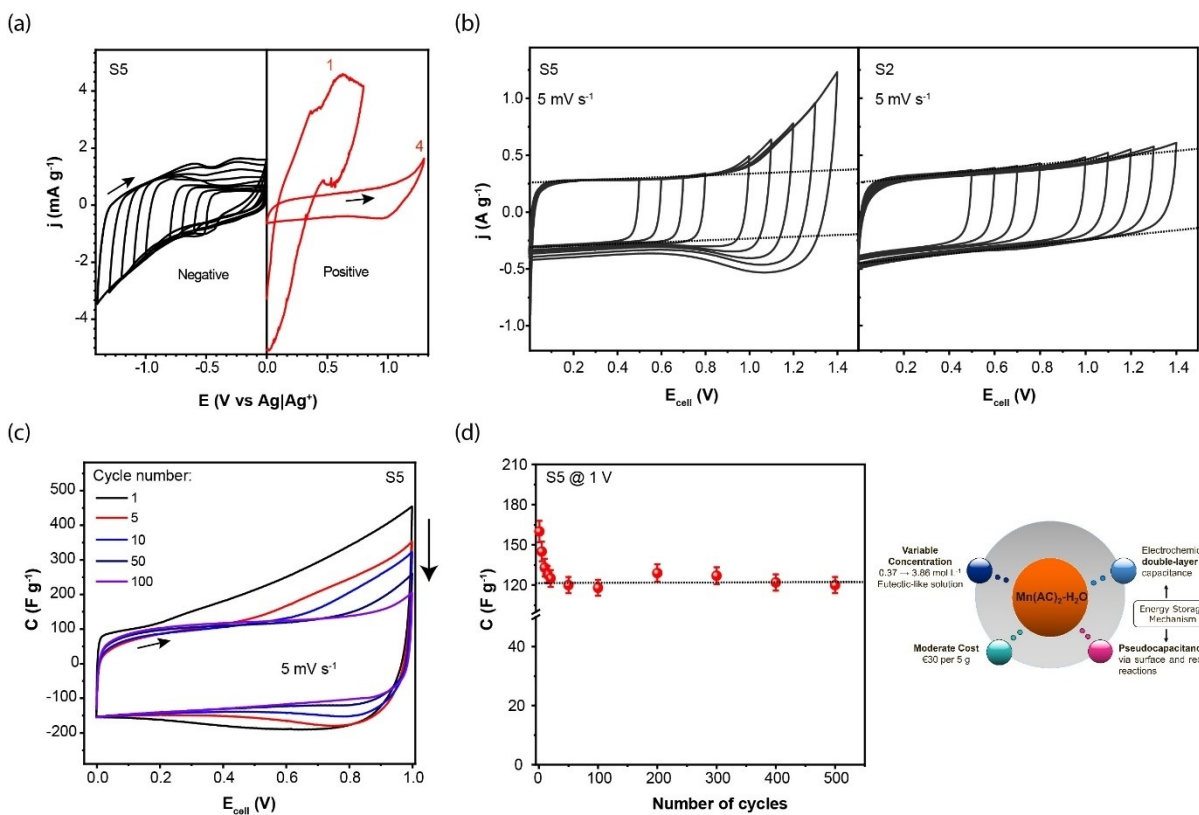
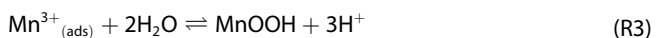
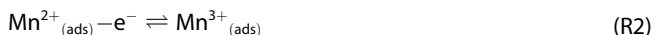


Figure 7. (a) Three-electrode cyclic voltammetry profiles of the two-electrode symmetric supercapacitor in the S5 solution. The scan rate is 5 mV s⁻¹. (b) Cyclic voltammetry profiles of the supercapacitor at different prolonged electrochemical windows in the presence of the S5 and S2 solutions. (c) Cyclic voltammetry of the two-electrode symmetric supercapacitor under different cycle numbers. (d) Specific capacitance as a function of cycles derived from the voltammograms at 1.0 V vs Ag/Ag⁺. The schematic on the right-hand side outlines the traits of manganese acetate hydrate solutions in energy storage applications.

cations^[13] and is catalyzed by the acetate anions. The pH for aqueous solutions of manganese(II) acetate tetrahydrate is ca. 7.0 (50 g L⁻¹, H₂O, 20 °C). In these mild conditions, the deprotonated acetate anions are adsorbed to the activated carbon cathode and promote the formation of MnO₂ (Figure 8). This reaction has been reported in neutral and weakly acidic environments^[16] and follows the PECC mechanism (physical-electrochemical-chemical-chemical) detailed below (R1→R4):



Under repetitive CV cycles the oxidative current diminishes since the deposition of MnO₂ on the surface of the activated carbon (R3 and R4) under longer timeframes reduces the dismutation of the Mn³⁺ ions (i.e., the reduction of Mn³⁺ to Mn²⁺ is favoured over the oxidation to MnO₂) and gives way to a more box-like CV that describes the pseudo-capacitance of the Mn³⁺/Mn²⁺ pair (Figure 7c, R2).

This is the case for supercapacitive devices with all solutions (Figure S2). The specific capacity gleaned from the voltammograms is given by the following equation^[68] and corroborates the proposed reaction scheme.

$$C = \int \frac{i \times dt}{m \times \Delta E} \quad (12)$$

The faradaic reactions (R1) contribute to a high initial specific capacity (i.e., 180 F g⁻¹, measured through an *E*_{cell} of 1.0 V, Figure 7d) followed by a decrease within the first ~80 cycles and a subsequent stabilization at 122 F g⁻¹. The deposition of MnO₂ reduced the accessible surface area (i.e., blocking of active sites on the cathode's surface) and led to the stabilization of the specific capacity. It should be noted here that the higher specific capacitance of Figure 7d against Figure 7c is due to the bigger *E*_{cell}, viz. 1.0 vs 1.4 V.

Further evidence of the reversibility of the Mn²⁺/MnO₂ redox couple comes from a recent study on a zinc-manganese battery in the presence of acetate anions.^[14] A manganese acetate neutral electrolyte led to a liquid-solid reaction of Mn²⁺/MnO₂ couple via the coordination effect of acetate (CH₃COO⁻) on Mn²⁺ (R5), supporting the direct deposition of MnO₂ on the positive electrode without the generation of Mn³⁺ since the acetate ligand hinders the parasitic disproportion of Mn³⁺ ions.

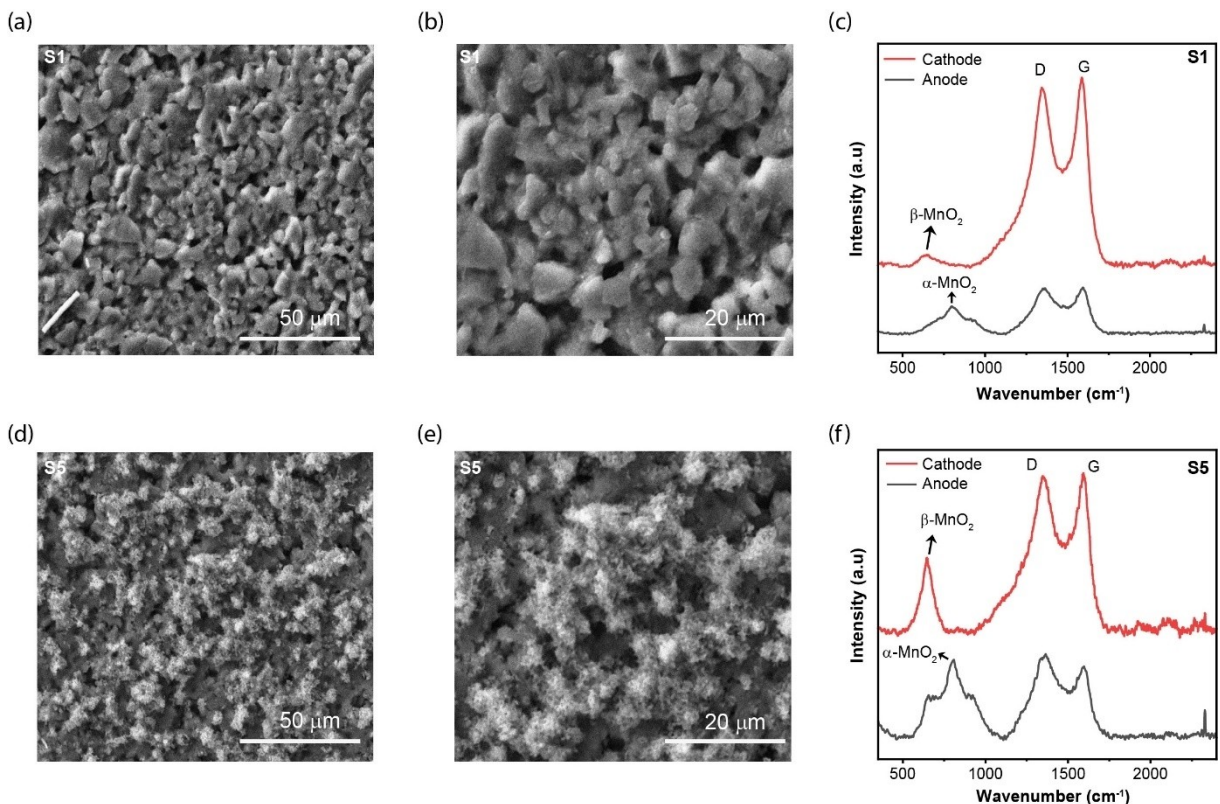
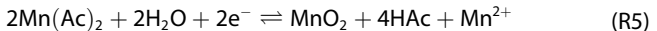


Figure 8. SEM micrographs of cycled activated carbon surfaces ($\times 500$ and $\times 2000$) after consecutive CV cycling on a two-electrode symmetric supercapacitor in the presence of S1 (a) (b) and S5 (d) (e) solutions. (c) (f) Raman spectra of the activated carbon anode and cathodes of the two-electrode symmetric supercapacitor under the different solutions.



To this end, the positive and negative electrodes of the supercapacitors containing the S1 and S5 electrolytes were analyzed through ex-situ scanning electron microscopy, X-ray diffraction and Raman spectroscopy (Figure 8). The SEM images (Figures 8a–b, Figures 8d–e) reveal a highly porous and irregular surface structure, characteristic of an activated carbon electrode.^[23] The carbon matrix appears as a network of irregularly shaped voids, channels and particles that encompass the clusters or particles of MnO_2 adhering to the carbon surface. Besides, the Raman spectra confirm the presence of manganese oxides^[69] (viz., α and β phase of MnO_2 , also corroborated in the XRD spectra depicted in Figure S3a) on both the anode and cathode of the supercapacitor. The difference in the intensity of MnO_2 between Figures 8c and 8f is quite significant, stressing the effect of salt concentration on the deposition of manganese at the cathode (Table 1, S1 vs S5).

Moreover, the D and G peaks originating from the activated carbon are evident. The I_D/I_G ratio^[70] for the cathode is higher than the one for the anode in both cases (2.11 vs 1.68 for the supercapacitor with S1; 2.68 vs 2.21 for the supercapacitor with S5), suggesting a higher quantity of defects within the carbon atom crystals (due to R1 and R2), that is a greater presence of sp^3 hybridized carbon atoms. The full width at half maximum (FWHM) values of the cathodes are higher (i.e., the Raman peak is broader) than those of the anodes, viz., 111.1 vs 105.8 cm^{-1}

for S1 and 107.5 vs 100.5 cm^{-1} for S5, further pointing out the greater degree of disorder and structural changes of the activated carbon, for both devices. The separators of the devices under FT-IR revealed typical spectra of glass microfibre filter paper^[23] (Figure S3b).

To delve deeper into whether the acetate anion holds a specific catalytic role in the reversible liquid/solid MnO_2 deposition reaction, cyclic voltammograms (2 mV s⁻¹) of different aqueous electrolytes with different manganese-based salts under saturation ($[\text{MnSO}_4] = 3.5 \text{ mol L}^{-1}$, $[\text{Mn}(\text{NO}_3)_2] = 4.5 \text{ mol L}^{-1}$, $[\text{Mn}(\text{Ac})_2] = 3.8 \text{ mol L}^{-1}$) were carried out (Figure 9a). Only the voltammogram with the manganese acetate exhibits signs of the MnO_2 deposition at 1.4 V, with the specific capacitance reaching 255 F g⁻¹. As the scan rate increases, the specific capacitance stabilizes around 180 F g⁻¹ for $\text{Mn}(\text{Ac})_2$, markedly higher than the other two saturated manganese-based solutions (i.e., 120 F g⁻¹, Figure 9b).

Molecular simulations on these salts (Figure S4), i.e., four electrolyte systems; Mn^{2+} , $4\text{H}_2\text{O}$ and X with and without anions where X denotes NO_3^- , SO_4^{2-} and CH_3COO^- , revealed the partial charges (δ) on the Mn^{2+} cation and the energy levels of the HOMO and LUMO boundary orbitals, summarized in Table 5.

The water molecules in the hydration shell interact with the Mn^{2+} , forming coordinate bonds with the cation, i.e., the partial charge on the Mn^{2+} cation goes down. Here, the hydration and anion complexation significantly reduce the partial load on the

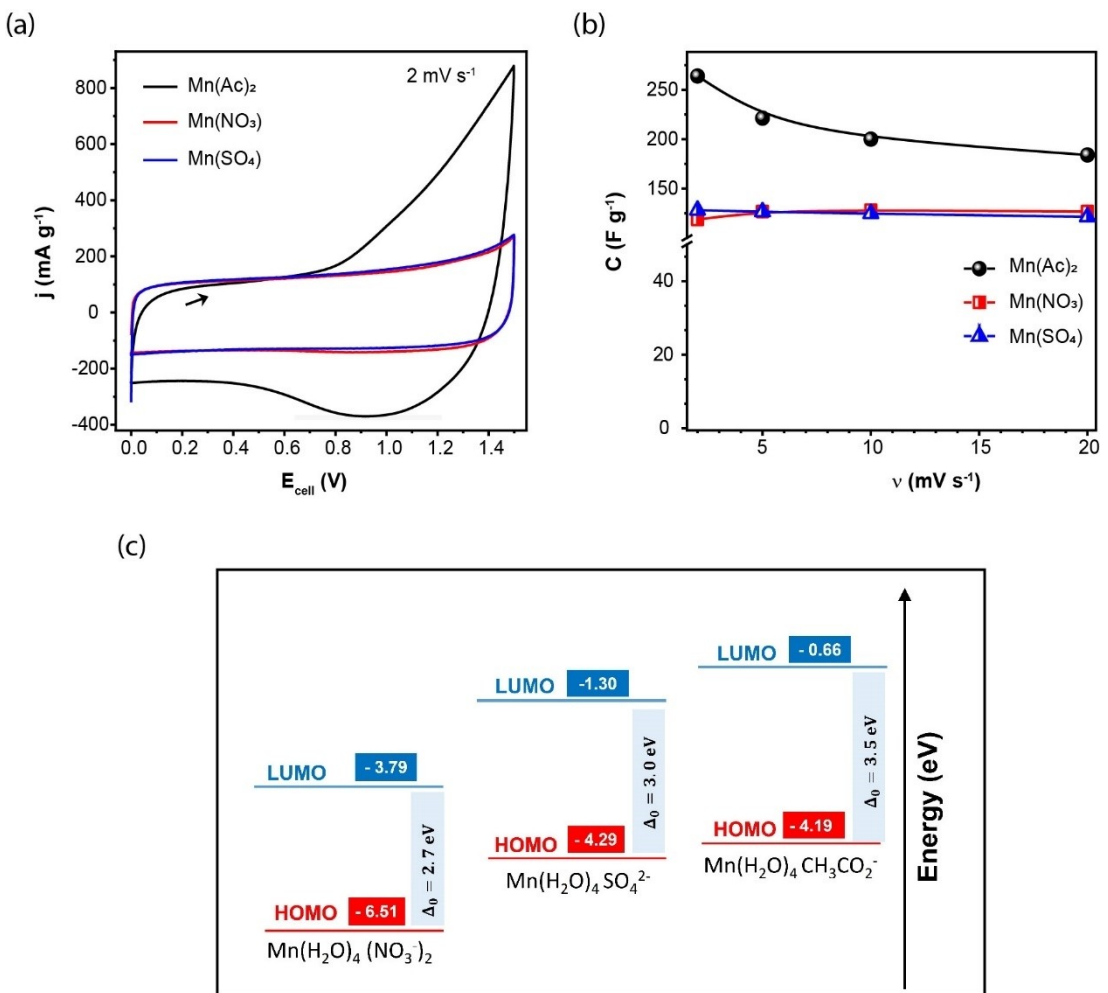


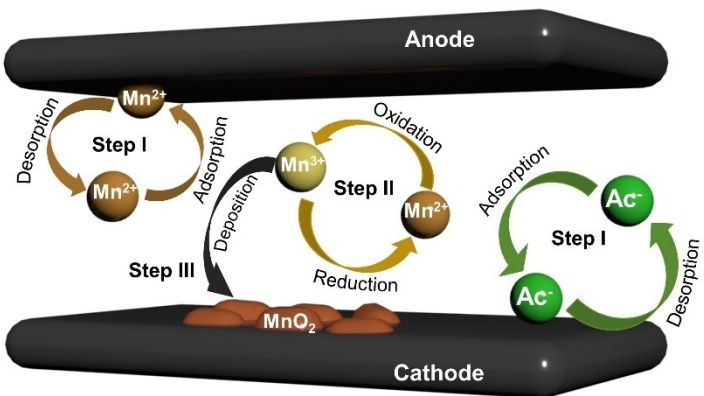
Figure 9. (a) Cyclic voltammetry profiles of the two-electrode symmetric supercapacitors under different manganese salts. The scan rate is 2 mV s⁻¹. (b) Specific capacitance as a function of scan rate. (c) Highest occupied molecular orbital (HOMO) and lowest unoccupied molecular orbital (LUMO) energy levels of the manganese acetate-water solutions comprising different manganese-salts.

Table 5. Theoretical calculations of partial charge, δ , HOMO-LUMO energy (eV) and ΔE gap (eV) of hydrated manganese salts (MnX ; $X = NO_3^-$, SO_4^{2-} and $CH_3CO_2^-$).					
Electrolyte	Partial charge of Mn^{2+} (δ)	Partial charge of anion X^- (δ)	HOMO (eV)	LUMO (eV)	ΔE (eV)
$Mn^{2+}(H_2O)_4$	+0.884	–	–14.98	–11.89	3.1
$Mn^{2+}(H_2O)_4; 2NO_3^-$	+0.338	–0.54	–6.51	–3.79	2.7
$Mn^{2+}(H_2O)_4; SO_4^{2-}$	+0.158	–0.62	–4.29	–1.23	3.0
$Mn^{2+}(H_2O)_4; 2CH_3CO_2^-$	–0.198	–0.35	–4.19	–0.66	3.5

Mn^{2+} cation. In the presence of $4H_2O$, Mn^{2+} is partially charged ($\delta \sim 0.9$). The point charge, initially +2, is reduced by a factor of 2.5 when nitrate anions are present and by a factor of 5.5 when sulfate anions are present. When acetate anions are present, the cation charge is completely masked by the bidentate COO^- ligands whose partial charge, δ^- is lower than in NO_3^- or SO_4^{2-} (Table 5). The gap ΔE (eV) between the HOMO and LUMO manifests a stabilization of the $Mn^{2+}Xn^-$ couple in an aqueous environment in the order $NO_3^- < SO_4^{2-} < CH_3CO_2^-$ (Figure 9c). NO_3^- is a relatively simple and small anion and does

not have strongly interacting lone pairs with Mn^{2+} . The other anions are larger with multiple oxygen atoms containing lone pairs that interact more strongly with the Mn^{2+} cations leading to higher gap ΔE values.

Thus, based on the aforementioned observations, we propose the following mechanism (Scheme 1). The acetate ligand adsorbs to the surface of the positively polarized activated carbon (step I), leaving the Mn^{2+} cation to freely oxidize reversibly at the electrode (step II) with the competing deposition reaction of MnO_2 (step III). After the activated carbon



Scheme 1. Schematic portraying the energy conversion and storage mechanisms of a two-electrode symmetric AC (activated carbon)//AC supercapacitor comprising a (concentrated) $\text{Mn}(\text{Ac})_2\text{-H}_2\text{O}$ electrolyte. Mechanisms involved: Step I; electrochemical double-layer capacitance. Step II and Step III; pseudocapacitance via surface redox reactions.

is covered with a layer of MnO_2 , the reversible pseudocapacitive storage prevails as depicted in the rectangular voltammograms of Figures 7 and Figure S2. In the presence of nitrate and sulphate ions, steps II and III are not observed and the capacitive mechanism (i.e., adsorption of the ions on the activated carbon of the two electrodes) is absent. This scenario is particularly notable for low concentrations of $\text{Mn}(\text{Ac})_2$ salt ($[\text{S1}] = 0.37 \text{ mol L}^{-1}$ and $[\text{S2}] = 0.87 \text{ mol L}^{-1}$).

2.2.2. Electrochemical performance of the two-electrode symmetric supercapacitor

Figure 10a shows typical galvanostatic charge-discharge curves of the symmetric two-electrode supercapacitor in the presence of the different salt concentrations at a current density of 0.8 A g^{-1} . Solutions S1 to S3 feature the conventional triangle-shaped charge/discharge curves reaching a total cell voltage of

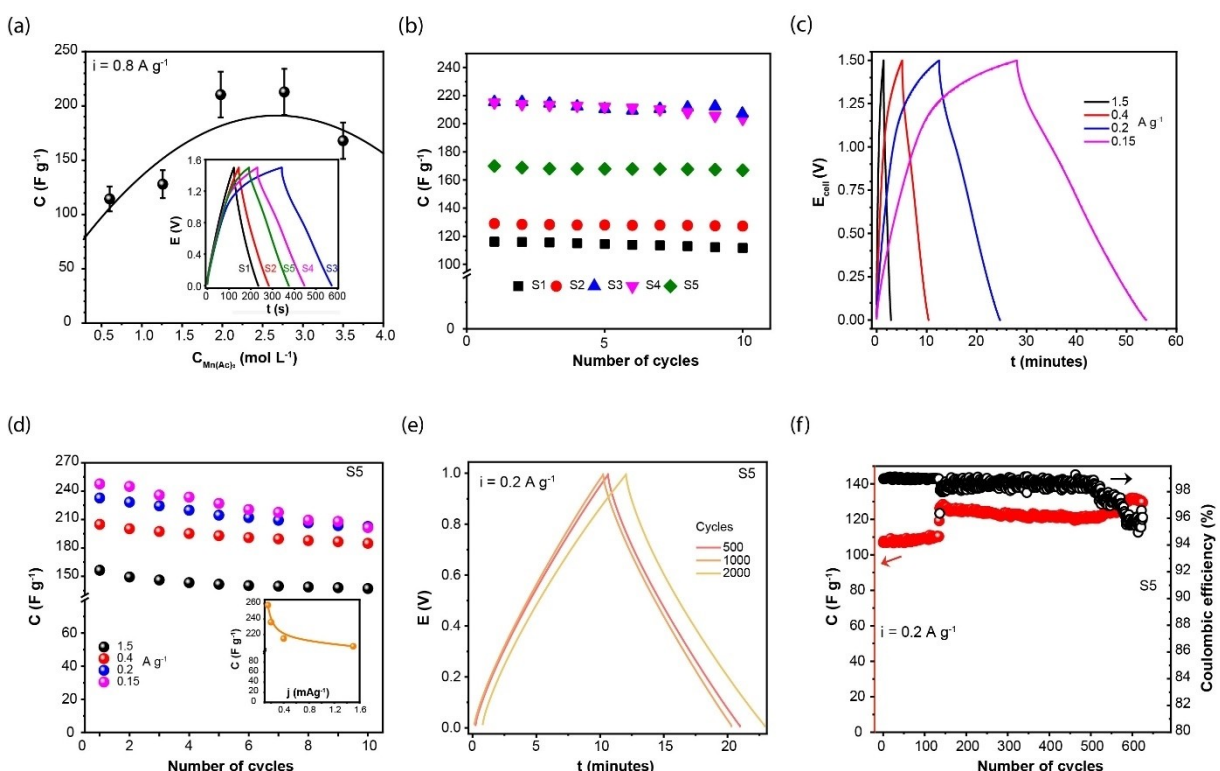


Figure 10. (a) Specific capacitance as a function of manganese acetate concentration. Inset shows the galvanostatic charge-discharge curves of a symmetric two-electrode supercapacitor in different $\text{Mn}(\text{AC})_2\text{-H}_2\text{O}$ solutions at 0.8 F g^{-1} . (b) First ten cycles stemmed from the GCD at 0.8 F g^{-1} . (c) Galvanostatic charge-discharge curves of the two-electrode symmetric supercapacitor in the S5 solution at different current densities. (d) Specific capacitance for the first ten cycles at different current densities for the supercapacitor in the presence of the S5 solution. (e) Charge-discharge profile as a function of cycle number for the supercapacitor with S5 under 0.2 A g^{-1} . (f) Specific capacitance retention and coulombic efficiency under long-term cycling. All measurements were performed at 25°C .

1.5 V. The specific capacitance (C) evolved from the linear part of the discharge curve^[65] for 20 cycles is given in Figure 10b. The C values increase with higher salt concentration (S1→S4) while for S5 (saturated solution) they linger at 170 F g⁻¹. During the first cycles, MnO₂ deposition is favourable (Scheme 1) between 1.5 mol L⁻¹ (S3) and 2.5 mol L⁻¹ (S4) of manganese. Then, it decreases possibly due to the formation of Mn³⁺ cations and their partial migration to the anode. Overall, S5 seems to be more stable during the initial cycling process at the same current density (0.8 A g⁻¹). As expected, an increase from 0.15 to 1.5 A g⁻¹ leads to a decrease of the specific capacitance, i.e., from 260 to 150 F g⁻¹ (Figures 10c-d and Figure S5 for the rest solutions), indicating that the pseudocapacitive mechanism (i.e., Mn²⁺↔Mn³⁺) is kinetically controlled and depends on the transfer rate of the electron. The storage mechanism appears as purely capacitive within an operating voltage of less than 1.0 V as seen in Figure 7b (and Figure 10e), regardless of concentration and scan rate. It becomes partially pseudocapacitive for voltages greater than 1.0 V. The pseudocapacitive contribution to the total capacitance hinges on the electronic transfer kinetics as well as concentration and operating voltage. At a cell voltage of 1.5, the pseudocapacitance contribution can be extracted from the inset of Figure 10d, taking into account that at somewhat high current densities (1.5 A g⁻¹) only the purely capacitive (non-faradic) contribution is present.

The pseudo-capacitive contribution value, $\alpha(\%) = \frac{C_{sp}^T - C_{sp}^0}{C_{sp}^T} \times 100$, where C_{sp}^T , C_{sp}^0 , and $(C_{sp}^T - C_{sp}^0)$ denote the total capacity, pure capacitive and pseudocapacitive parts, respectively, are extracted from figure 10d and presented in Table 6

Regarding the robustness of this energy storage device, the long-term cycling measurements (Figure 10e) for the concentrated solution S5 revealed a stable specific capacitance (Fig-

ure 10f, 125 F g⁻¹ for an E_{cell} of 1.0 V) for 2000 cycles, which is followed by a drop in the coulombic efficiency (99→94%). At this current density, the deposition of manganese (i.e., the pseudocapacitive part of the Mn²⁺ ions storage) is not completely reversible which explains the low coulombic efficiency. What is more, the equivalent series resistance (ESR) stabilizes around 20 ohms (Figure S6). Interestingly, Figure 10 exposes an increase in the specific capacitance after the 150th cycle, probably due to an activation of the electrode(s), improved ion accessibility (stabilization of the electrolyte) or surface restructuring (i.e., deposition/dissolution of MnO₂ on the cathode surface).

The specific capacitance illustrated in Figure 10 aligns with reported values from other two-electrode symmetrical supercapacitors utilizing aqueous electrolytes (Table 7). The use of graphene, carbon nanotubes (CNT) or nanofibers seems to boost the specific capacitance attributed to their pore and surface morphology primarily (without taking into account the design of such electrodes). Supercapacitors using activated carbon (i.e., AC//Na(Ac)//AC) reported an inferior performance to this work.

Overall, the results underscore the suitability of manganese acetate electrolyte(s) for energy storage applications. What's more, these aqueous solutions can be considered green. In industrial processes like energy storage system manufacturing, adherence to green chemistry^[79] involves minimizing environmental impact in raw material acquisition, maintaining low toxicity across the life cycle, and prioritizing materials with high abundance and renewability (the three criteria^[79]), exemplified by manganese and carbon in this case. Likewise, the efficacy of green chemistry processes is tied to their capacity to minimize the requirement for diverse materials in product manufacturing, known as atom economy. In this regard, the utilization of this salt fulfills the three criteria by streamlining the cathode preparation stages and supercapacitor assembly. This approach restricts the types of elements to be recycled within the system (i.e., Mn, C), thereby diminishing the environmental impact.

Table 6. The contribution of pseudo capacitance at each current density calculated from equation 12.

j (mA g ⁻¹)	0.15	0.2	0.4	1.5
α (%)	40	37	25	0

Table 7. Comparison of specific capacitance at a set normalized current density for carbon/manganese oxide-based hybrid systems in different aqueous electrolytes.

System	Electrolyte	j (A g ⁻¹)	C (F g ⁻¹)	Ref
MnO ₂ -CNT//AC	0.5 M Na ₂ SO ₄	1	110	[73]
MnO ₂ //AC	1 mol L ⁻¹ Na ₂ SO ₄	0.1	160	[68]
MnO ₂ -CNT//AC	2 mol L ⁻¹ KNO ₃	0.1	140	[74]
MnO ₂ -CNT//AC	1 mol L ⁻¹ Li ₂ SO ₄	0.5	160	[75]
Graphene-MnO ₂ //Graphene	1 mol L ⁻¹ Na ₂ SO ₄	1	200	[76]
Graphene-MnO ₂ //AC-nanofiber	1 mol L ⁻¹ Na ₂ SO ₄	3	160	[77]
MnO ₂ /rGO	PVA/H ₃ PO ₄ -gel	2	240	[78]
AC//AC	0.5 mol L ⁻¹ Na(Ac)	0.2	90	[72]
AC-MnO ₂ //AC	2 mol L ⁻¹ Mn(Ac) ₂	0.2	~130	[this work]

3. Conclusions

In conclusion, this study explored the feasibility of aqueous manganese acetate electrolytes for energy storage applications. It delved into eutectic behaviour, volumetric and transport properties of $\text{Mn}(\text{Ac})_2\text{-H}_2\text{O}$ solutions, revealing higher eutectic depth (ΔT) compared to $\text{Mn}(\text{NO}_3)_2\text{-H}_2\text{O}$. Volumetric properties indicated strong interactions and thermodynamic properties reflected reorganization under temperature variation. Transport properties, including dynamic viscosity and ionic conductivity, provided insights into solution behaviour (i.e., monotonic vs. fluctuating increase in conductivity with temperature). The study applied $\text{Mn}(\text{Ac})_2$ solutions in supercapacitors, showcasing a reversible MnO_2 deposition reaction at the cathode influenced by acetate anions. Molecular simulations emphasized acetate's role, revealing its impact on electrochemical behaviour. A concentrated solution demonstrated moderate performance and stability over 2000 cycles for a concentrated solution (3.86 mol L^{-1}) with the concurring deposition of the MnO_2 layer on the cathode partially affecting the specific capacitance (125 F g^{-1}) and coulombic efficiency (94–99%), suggesting the potential of manganese acetate hydrate solutions in green electrolytes for advanced energy storage systems.

Acknowledgements

The authors would like to thank "La Région Centre Val de Loire" for financial support.

Conflict of Interests

The authors declare that they have no known competing financial interests or personal relationships that could have appeared to influence the work reported in this paper.

Data Availability Statement

The data that support the findings of this study are available in the supplementary material of this article.

Keywords: Electrolyte • Eutectic • Manganese acetate • Manganese dioxide • Supercapacitor

- [1] A. N. Kay Lup, V. Soni, B. Keenan, J. Son, M. R. Taghartapeh, M. M. Morato, Y. Poya, R. M. Montañés, *Environmental Science: Advances*. 2023, 2, 570–585.
- [2] L. Wang, Y. Deng, L. Yan, *ACS Appl. Energ. Mater.* 2023, 6, 10585–10592.
- [3] S. Zhang, X. Shi, X. Chen, D. Zhang, X. Liu, Z. Zhang, P. K. Chu, T. Tang, E. Mijowska, *ACS Appl. Energ. Mater.* 2019, 2, 4234–4243.
- [4] M. Yao, X. Ji, T.-F. Chou, S. Cheng, L. Yang, P. Wu, H. Luo, Y. Zhu, L. Tang, J. Wang, M. Liu, *ACS Appl. Energ. Mater.* 2019, 2, 2743–2750.
- [5] C. Mevada, M. Mukhopadhyay, *Ind. Eng. Chem. Res.* 2021, 60, 1096–1111.
- [6] M. Maher, B. Yousif, M. E. A. Abo-Elsoud, S. Hassan, *J. Mater. Sci. Mater. Electron.* 2021, 32, 27721–27743.

- [7] F. Wang, X. Wu, X. Yuan, Z. Liu, Y. Zhang, L. Fu, Y. Zhu, Q. Zhou, Y. Wu, W. Huang, *Chem. Soc. Rev.* 2017, 46, 6816–6854.
- [8] N. M. Keppetipola, M. Dissanayake, P. Dissanayake, B. Karunaratne, M. A. Dourges, D. Talaga, L. Servant, C. Olivier, T. Toupance, S. Uchida, K. Tennakone, G. R. A. Kumara, L. Cojocaru, *RSC Adv.* 2021, 11, 2854–2865.
- [9] X. Ji, H. Luo, W. Dong, L. Yang, J. Guo, S. Cheng, *Electrochim. Acta*. 2023, 449, 142172.
- [10] C. C. H. Tran, J. Santos-Peña, C. Damas, *Electrochim. Acta*. 2020, 335, 135564.
- [11] H. Wang, T. Wang, G. Stevenson, M. Chamoun, R. W. Lindström, *Energy Storage Mater.* 2023, 63, 103008.
- [12] A. Thompson, *Sci. Light* 2023, 2023, 211101.
- [13] J. Lei, L. Jiang, Y.-C. Lu, *Chemical Physics Reviews*. 2023, 4, 021307.
- [14] C. Xie, T. Li, C. Deng, Y. Song, H. Zhang, X. Li, *Energy Environ. Sci.* 2020, 13, 135–143.
- [15] B. Dyatkin, V. Presser, M. Heon, M. R. Lukatskaya, M. Beidaghi, Y. Gogotsi, *ChemSusChem*. 2013, 6, 2269–2280.
- [16] A. Biswal, B. Chandra Tripathy, K. Sanjay, T. Subbaiah, M. Minakshi, *RSC Adv.* 2015, 5, 58255–58283.
- [17] K. Wickramaarachchi, M. Minakshi, *J. Energy Storage* 2022, 56, 106099.
- [18] Y. Xue, Y. Wang, *Green Chem.* 2020, 22, 6288–6309.
- [19] Z. Fan, J. Chen, B. Zhang, F. Sun, B. Liu, Y. Kuang, *Mater. Res. Bull.* 2008, 43, 2085–2091.
- [20] T. Ishihara, A. Kawahara, H. Nishiguchi, M. Yoshio, Y. Takita, *J. Power Sources*. 2003, 119–121, 24–27.
- [21] X. Zeng, J. Liu, J. Mao, J. Hao, Z. Wang, S. Zhou, C. D. Ling, Z. Guo, *Adv. Energy Mater.* 2020, 10, 1904163.
- [22] M. Raghibi, G. Nikiforidis, M. Anouti, *ChemElectroChem*. 2023, 10, e202300183.
- [23] G. Nikiforidis, M. E. Yagoubi, M. Anouti, *Electrochim. Acta*. 2022, 402, 139529.
- [24] G. Nikiforidis, S. Phadke, M. Anouti, *Adv. Mater. Interfaces* 2023, 10, 2202046.
- [25] M. A. Mohamed, S. A. Halawy, *Thermochim. Acta*. 1994, 242, 173–186.
- [26] T. S. Sheriff, M. Watkinson, M. Mottevalli, J. F. Lesin, *Dalton Trans.* 2010, 39, 53–55.
- [27] Y. Marcus, *ACS Sustainable Chem. Eng.* 2017, 5, 11780–11787.
- [28] E. L. Smith, A. P. Abbott, K. S. Ryder, *Chem. Rev.* 2014, 114, 11060–11082.
- [29] K. Iwase, Y. Nagano, I. Yoshikawa, H. Houjou, Y. Yamamura, K. Saito, *J. Phys. Chem. C*. 2014, 118, 27664–27671.
- [30] K. Iwase, Y. Toyama, I. Yoshikawa, Y. Yamamura, K. Saito, H. Houjou, *Bull. Chem. Soc. Jpn.* 2018, 91, 669–677.
- [31] C.-Y. Cheng, S.-L. Wang, *Acta Crystallogr. Sect. C* 1991, 47, 1734–1736.
- [32] K. Goossens, K. Lava, C. W. Bielawski, K. Binnemans, *Chem. Rev.* 2016, 116, 4643–4807.
- [33] T. Kato, J. Uchida, T. Ichikawa, T. Sakamoto, *Angew. Chem. Int. Ed.* 2018, 57, 4355–4371.
- [34] G. Lu, J. Yao, H. Li, *J. Chem. Eng. Data*. 2019, 64, 4264–4271.
- [35] B. K. Xiong, M. Paillot, M. Anouti, *J. Chem. Eng. Data*. 2020, 66, 4436.
- [36] T. F. Irvine, M. R. Duignan, *Int. Commun. Heat Mass Transfer* 1985, 12, 465–478.
- [37] L. Glasser, *Thermochim. Acta*. 2004, 421, 87–93.
- [38] H. D. B. Jenkins, D. Tudela, L. Glasser, *Inorg. Chem.* 2002, 41, 2364–2367.
- [39] H. D. B. Jenkins, L. Glasser, *Inorg. Chem.* 2002, 41, 4378–4388.
- [40] V. Philippe in *Thermodynamics of Hydration in Minerals: How to Predict These Entities*, Vol. (Ed. M.-R. Ricardo), IntechOpen, Rijeka, 2012, pp.Ch. 13.
- [41] M. Aniya, M. Ikeda in *A Model for Non-Arrhenius Ionic Conductivity*, Vol. 9 (Ed. Eds.: Editor), City, 2019.
- [42] J. Chidiac, L. Timperman, M. Anouti, *J. Energy Chem.* 2022, 65, 352–366.
- [43] P. G. Brewer, E. T. Peltzer, K. Lage, *Deep Sea Research Part I: Oceanographic Research Papers*. 2021, 176, 103592.
- [44] G. E. Walrafen, *J. Chem. Phys.* 2004, 40, 3249–3256.
- [45] J. C. Kistemaker, A. S. Lubbe, E. A. Bloemsma, B. L. Feringa, *ChemPhysChem*. 2016, 17, 1819–1822.
- [46] W. Good, D. B. Ingham, *Electrochim. Acta*. 1975, 20, 57–61.
- [47] N. Martinus, D. Crawford, D. Sinclair, C. A. Vincent, *Electrochim. Acta*. 1977, 22, 1183–1187.
- [48] Y. R. Dougassa, J. Jacquemin, L. El Ouatani, C. Tessier, M. Anouti, *J. Phys. Chem. B* 2014, 118, 3973–3980.
- [49] M. Kaminsky, *Z. Phys. Chem.* 1956, 8, 173–191.
- [50] R. S. Patil, V. R. Shaikh, P. D. Patil, A. U. Borse, K. J. Patil, *J. Mol. Liq.* 2014, 200, 416–424.
- [51] Y. Shao, K. Shigenobu, M. Watanabe, C. Zhang, *J. Phys. Chem. B*. 2020, 124, 4774–4780.

- [52] L. Jiang, D. Dong, Y.-C. Lu, *Nano Research Energy*. **2022**, *1*, e9120003.
- [53] J. Chidiac, G. Nikiforidis, L. Timperman, M. Anouti, *ChemPhysChem*. **2022**, *23*, e202200224.
- [54] O. Okoturo, T. VanderNoot, *J. Electroanal. Chem.* **2004**, *568*, 167–181.
- [55] S. Amara, W. Zaidi, L. Timperman, G. Nikiforidis, M. Anouti, *J. Chem. Phys.* **2021**, *154*, 164708.
- [56] S. C. Sahoo, M. Dubey, M. A. Alam, M. Ray, *Inorg. Chim. Acta*. **2010**, *363*, 3055–3060.
- [57] C. A. Angell, *Chem. Rev.* **2002**, *102*, 2627–2650.
- [58] C. A. Angell, R. D. Bressel, J. L. Green, H. Kanno, M. Oguni, E. J. Sare, *J. Food Eng.* **1994**, *22*, 115–142.
- [59] A. Boisset, L. Athouël, J. Jacquemin, P. Porion, T. Brousse, M. Anouti, *J. Phys. Chem. C*. **2013**, *117*, 7408–7422.
- [60] K. R. Harris, *J. Phys. Chem. B*. **2019**, *123*, 7014–7023.
- [61] C. Schreiner, S. Zugmann, R. Hartl, H. J. Gores, *J. Chem. Eng. Data*. **2010**, *55*, 1784–1788.
- [62] M. G. McLin, C. A. Angell, *J. Phys. Chem.* **1991**, *95*, 9464–9469.
- [63] W. Xu, E. I. Cooper, C. A. Angell, *J. Phys. Chem. B*. **2003**, *107*, 6170–6178.
- [64] R. Caminiti, P. Cucca, M. Monduzzi, G. Saba, G. Crisponi, *J. Chem. Phys.* **1984**, *81*, 543–551.
- [65] S. Wustoni, G. Nikiforidis, D. Ohayon, S. Inal, Y. S. Indartono, V. Suendo, B. Yuliarto, *Chem. Asian J.* **2022**, *17*, e202200427.
- [66] J. Sun, L. Guo, X. Sun, J. Zhang, L. Hou, L. Li, S. Yang, C. Yuan, *Batteries & Supercaps*. **2019**, *2*, 820–841.
- [67] G. Nikiforidis, S. Wustoni, D. Ohayon, V. Druet, S. Inal, *ACS Appl. Energ. Mater.* **2020**, *3*, 7896–7907.
- [68] X. Zhang, P. Yu, H. Zhang, D. Zhang, X. Sun, Y. Ma, *Electrochim. Acta*. **2013**, *89*, 523–529.
- [69] N. Mironova-Ulmane, A. Kuzmin, V. Skvortsova, G. Chikvaidze, I. Sildos, J. Grabis, D. Jankoviča, A. Dindune, M. Mairov, *Acta Phys. Pol. A*. **2018**, *133*, 1013–1016.
- [70] G. Nikiforidis, J. Pires, S. Phadke, M. Anouti, *ChemElectroChem*. **2022**, *9*, e202200571.
- [71] T. Schoetz, L. W. Gordon, S. Ivanov, A. Bund, D. Mandler, R. J. Messinger, *Electrochim. Acta*. **2022**, *412*, 140072.
- [72] J. Piwek, A. Platek, K. Fic, E. Frackowiak, *Electrochim. Acta*. **2016**, *215*, 179–186.
- [73] L. Demarconnay, E. Raymundo-Piñero, F. Béguin, *J. Power Sources*. **2011**, *196*, 580–586.
- [74] V. Khomenko, E. Raymundo-Piñero, F. Béguin, *J. Power Sources*. **2006**, *153*, 183–190.
- [75] F. Ochai-Ejeh, M. J. Madito, K. Makgopa, M. N. Rancho, O. Olaniyan, N. Manyala, *Electrochim. Acta*. **2018**, *289*, 363–375.
- [76] Z.-S. Wu, W. Ren, D.-W. Wang, F. Li, B. Liu, H.-M. Cheng, *ACS Nano*. **2010**, *4*, 5835–5842.
- [77] Z. Fan, J. Yan, T. Wei, L. Zhi, G. Ning, T. Li, F. Wei, *Adv. Funct. Mater.* **2011**, *21*, 2366–2375.
- [78] L. Peng, X. Peng, B. Liu, C. Wu, Y. Xie, G. Yu, *Nano Lett.* **2013**, *13*, 2151–2157.
- [79] P. T. Anastas, R. L. Lankey, *Green Chem.* **2000**, *2*, 289–295.

Manuscript received: November 28, 2023

Revised manuscript received: January 16, 2024

Accepted manuscript online: January 17, 2024

Version of record online: February 2, 2024